

ARTICLE

<https://doi.org/10.1038/s41467-019-10982-8>

OPEN

Adhesion of two-dimensional titanium carbides (MXenes) and graphene to silicon

Yanxiao Li^{1,4}, Shuohan Huang^{2,4}, Congjie Wei¹, Chenglin Wu¹ & Vadym N. Mochalin^{ib} ^{2,3}

Two-dimensional transition metal carbides (MXenes) have attracted a great interest of the research community as a relatively recently discovered large class of materials with unique electronic and optical properties. Understanding of adhesion between MXenes and various substrates is critically important for MXene device fabrication and performance. We report results of direct atomic force microscopy (AFM) measurements of adhesion of two MXenes ($\text{Ti}_3\text{C}_2\text{T}_x$ and Ti_2CT_x) with a SiO_2 coated Si spherical tip. The Maugis-Dugdale theory was applied to convert the AFM measured adhesion force to adhesion energy, while taking into account surface roughness. The obtained adhesion energies were compared with those for mono-, bi-, and tri-layer graphene, as well as SiO_2 substrates. The average adhesion energies for the MXenes are $0.90 \pm 0.03 \text{ J m}^{-2}$ and $0.40 \pm 0.02 \text{ J m}^{-2}$ for thicker $\text{Ti}_3\text{C}_2\text{T}_x$ and thinner Ti_2CT_x , respectively, which is of the same order of magnitude as that between graphene and silica tip.

¹Department of Civil, Architectural, and Environmental Engineering, Missouri University of Science and Technology, Rolla, MO 65409, USA. ²Department of Chemistry, Missouri University of Science and Technology, Rolla, MO 65409, USA. ³Department of Materials Science and Engineering, Missouri University of Science and Technology, Rolla, MO 65409, USA. ⁴These authors contributed equally: Yanxiao Li, Shuohan Huang. Correspondence and requests for materials should be addressed to C.W. (email: wuch@mst.edu) or to V.N.M. (email: mochalinv@mst.edu)

A large family of two-dimensional (2D) transition metal carbides and nitrides (MXenes) have emerged over the past few years as a class of materials with superior and highly tunable electronic and optical properties^{1,2}. These properties render MXenes prospective materials for supercapacitors^{3,4}, Li-ion and beyond Li-ion batteries^{5,6}, triboelectric generators⁷, photonic diodes and Q-switched lasers⁸, sensors^{9,10}, composites^{11,12}, etc. More than 20 different MXenes have been synthesized by selective A element extraction with fluorine-containing etchants from bulk ternary compounds known as MAX phases^{1,13}. MXenes have a general formula $M_{n+1}X_nT_x$, where M represents an early transition metal (Ti, Zr, V, Nb, Ta, Cr, Mo, Sc, etc.), X is carbon or nitrogen, and n is an integer. T denotes the terminating functional groups (fluorine, hydroxyl, and other oxygen-containing groups) attached to MXene basal surfaces during synthesis^{14–16}. Among experimentally available MXenes, $Ti_3C_2T_x$ and Ti_2CT_x are some of the most widely investigated. MXenes are intrinsically hydrophilic and yet, they have demonstrated higher electrical conductivity than solution processed graphene¹⁷. In addition, their exceptional electrochemical properties show great promise for flexible electronics and planar devices¹⁸. There are studies on MXene dispersions in organic solvents for incorporation into polymers, inks, etc.¹⁹. As researchers move closer to device fabrication, adhesion to different materials, as well as other mechanical properties of MXenes become of greater importance. There is a handful of published data on the mechanical behavior of MXenes. Theoretical calculations using molecular dynamics (MD) have predicted the Young's modulus of 597 GPa for bare Ti_2C and 502 GPa for bare Ti_3C_2 MXenes²⁰, whereas a recent experimental AFM indentation study of a single suspended $Ti_3C_2T_x$ MXene flake reported the value of 333 ± 30 GPa²¹. Although no other experimental data for $Ti_3C_2T_x$ or Ti_2CT_x are available for comparison, the agreement between MD derived and experimental Young's modulus is fairly good, taking into account the defective structure and surface terminations in real MXene samples that have not been captured in the simulations. MD modeling has also predicted a high bending rigidity of MXenes compared to single atomic layer 2D materials like graphene and hexagonal BN²², an important result for the development of sensing applications of 2D materials. However, to our knowledge, no theoretical or experimental studies of adhesive properties of MXenes have been reported to date.

Nanoindentation has been widely used to characterize adhesion of thin films^{23–25}. In recent years, the adhesive interactions of monolayer and a few layer 2D materials have been intensively investigated. One of the important questions is to understand how the properties, in particular adhesive strength, change when transitioning from bulk to 2D form of a material. Answering this fundamental question will require systematic studies of the property (e.g., adhesive strength) while varying the thickness of a material without changing its atomic composition or type of bonding within the material. From this standpoint, the MXenes family represents another unique and still widely underutilized advantage, allowing to systematically change the thickness of the monolayer without changing the type of bonding or elemental composition of the material (e.g., going from Ti_2C to Ti_3C_2 to Ti_4C_3 , etc. within the same family of titanium carbide MXenes). Other 2D materials have fixed monolayer thickness and thus would not allow the systematic study of a property as a function of their monolayer thickness disentangled from other variables, such as elemental composition, chemical bonding, etc.

In this work, AFM was used to measure the adhesive properties of two MXenes ($Ti_3C_2T_x$, Ti_2CT_x), as well as the mono-layer, bi-layer, and tri-layer graphene interacting with the oxidized silicon tip. The force-displacement responses were evaluated and compared. The measured adhesion force was converted into the adhesion energy using the Maugis-Dugdale²⁶ theory and taking surface roughness into consideration. The experimentally measured adhesion energy between $Ti_3C_2T_x$ and SiO_2 is 0.90 ± 0.03 J m⁻², which is higher than that of Ti_2CT_x (0.40 ± 0.02 J m⁻²), thus the monolayer thickness was found to have a significant effect on the adhesion energy. However, in contrast to our experimental data for graphene, the number of MXene monolayers in a stacked MXene structure was found to have little impact on the adhesion energy.

Results

Surface profile. The surface roughness of the two types of MXene flakes was characterized using AFM scans in tapping mode with a 3 nm radius tip as shown in Fig. 1a. The RMS values for the MXene flake (Fig. 1b) are almost same as for SiO_2 surface, indicating that MXene flakes are very thin and conform closely to the substrate.

Typical line scans for MXene films of different thicknesses are shown in Fig. 2a for $Ti_3C_2T_x$ and Fig. 2b for Ti_2CT_x . The sharp

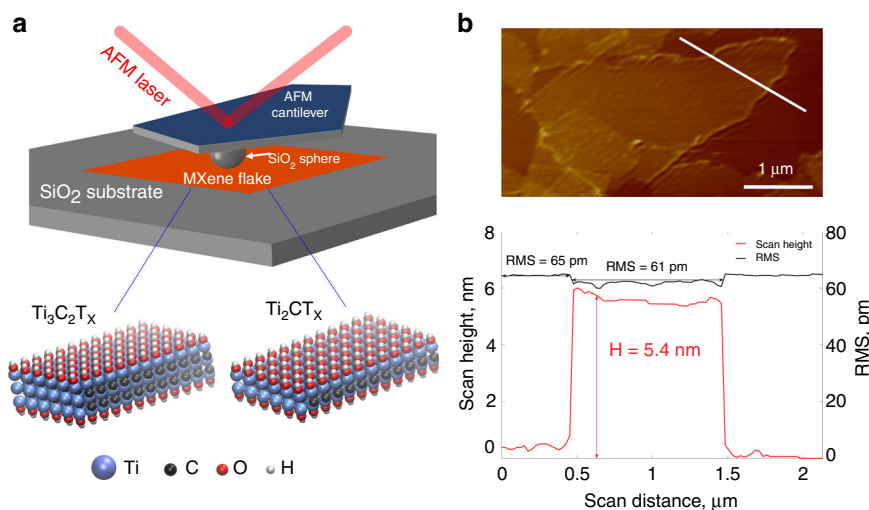


Fig. 1 **a** Schematic representation of AFM indentation experiment, **b** AFM image and surface profile along the white line across the $Ti_3C_2T_x$ flake deposited on SiO_2 coated Si substrate

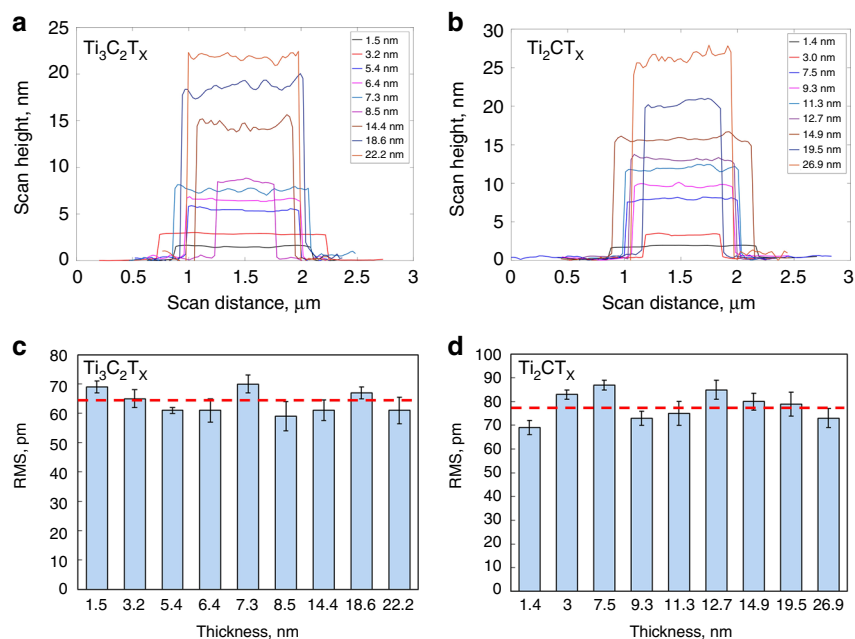


Fig. 2 AFM line scans (**a, b**) and corresponding RMS values (**c, d**) for $\text{Ti}_3\text{C}_2\text{T}_x$ and Ti_2CT_x films of different thicknesses. Horizontal dash lines in bottom panels represent the average RMS for $\text{Ti}_3\text{C}_2\text{T}_x$ and Ti_2CT_x , which were used in adhesion energy calculations. Error bars represent standard deviations in RMS values

changes in height at both sides of the line scans indicate the edges of the flakes. The horizontal length of the curves' plateaus gives the average size of the MXene flakes between the two edges. The average RMS values for $\text{Ti}_3\text{C}_2\text{T}_x$ and Ti_2CT_x films (excluding the potentially oxidized edges) with different thicknesses were calculated and presented in Fig. 2c, d, respectively. Compared with the corresponding average thickness, the RMS values are relatively low (59–70 pm for $\text{Ti}_3\text{C}_2\text{T}_x$, 69–87 pm for Ti_2CT_x) and within 5% of the corresponding thickness (compare top and bottom panels in Fig. 2), indicating relatively flat MXene surfaces. As follows from Fig. 2c, d, no clear thickness (i.e., the number of MXene monolayers) dependency was observed for the measured RMS values of the MXene films. The average RMS values were used in calculating the adhesion energies (below).

Force-displacement response. A typical force versus displacement response for tip approach and withdrawal measured on 5-monolayer $\text{Ti}_3\text{C}_2\text{T}_x$ sample is shown in Fig. 3a. At the start of the experiment, the AFM tip was at a large distance from the sample surface. As the tip approached the sample surface (I) (indicated by the black line starting from the left side of the graph), a slowly increasing negative force (adhesion) was measured. At a certain displacement value (II), the “jump-in” phenomenon was observed resulting from sudden bending of the AFM cantilever towards the sample surface as the adhesion reached its local maximum. After this, the AFM cantilever bending reduced with the continued displacement of the cantilever towards the sample until there was no negative load on the cantilever (at this point the cantilever is not bent) and the tip was in firm contact with the surface—this corresponds to the zero-displacement point (III); from here the indentation process begins upon further increase of displacement (IV). During the indentation stage, the tip experienced a positive force on it since the cantilever bends out of the sample surface (compare cartoons IV and II).

In the withdrawal process starting from the rightmost part of the graph in Fig. 3a (indicated by the red line), the force on the tip reduced during the tip retraction. At 0 nm displacement (i.e., zero-displacement point), there is now a pulling force acting on

the tip, which is balanced by its adhesion to the sample. When the displacement becomes slightly negative upon further withdrawal, the tip still adheres to the sample, resulting in cantilever bending towards the sample again (V). As the tip withdrawal continues, adhesion force approaches its maximum value before the tip “jumps-off” the sample surface (V to VI), turning the force acting on the cantilever into zero. The maximum adhesion force measured in point V ($-1.11 \mu\text{N}$ in Fig. 3a) was then used to calculate the adhesion energy between the tip and sample surface.

For all samples, the adhesion forces measured during the tip approach (-0.02 to $-0.42 \mu\text{N}$, Fig. 3b) are generally lower than those recorded in the withdrawal stage (-0.5 to $-1.56 \mu\text{N}$, Fig. 3c). The maximum adhesion force measured between the tip and monolayer graphene is much lower than that for bi-layer or tri-layer graphene (Fig. 3c). However, in contrast to graphene adhesion, no number-of-monolayer dependency of the maximum adhesion force was found for the MXene films. The maximum values of adhesion force are higher for $\text{Ti}_3\text{C}_2\text{T}_x$ ($1.07 \mu\text{N}$) than those for Ti_2CT_x ($0.53 \mu\text{N}$). The “jump-off” (V to VI) observed for graphene, as well as MXene samples describes adhesion with a large interaction range, which may be a sign of the capillary force effect. Similar findings were reported in the nanoindentation experiments conducted on the surface of graphene²⁷. The jump-off instability is worth mentioning at this conjunction as it might affect the accuracy of the measurements. However, this concern was eliminated by an accuracy analysis comparing the cantilever stiffness with the adhesion gradient during the experiment (Supplementary Note 1 and Supplementary Fig. 1). More force versus displacement data are provided in Supplementary Fig. 2. The average adhesion forces along with standard deviations for all samples are plotted in Supplementary Fig. 3a.

Adhesion energy. The adhesion energy was calculated from the measured “jump-off” (or maximum adhesion) force using the Maugis–Dugdale theory²⁸,

$$W_{\text{adh}} = \frac{F_{\text{adh}}}{\lambda\pi R_{\text{tip}}} \quad (1)$$

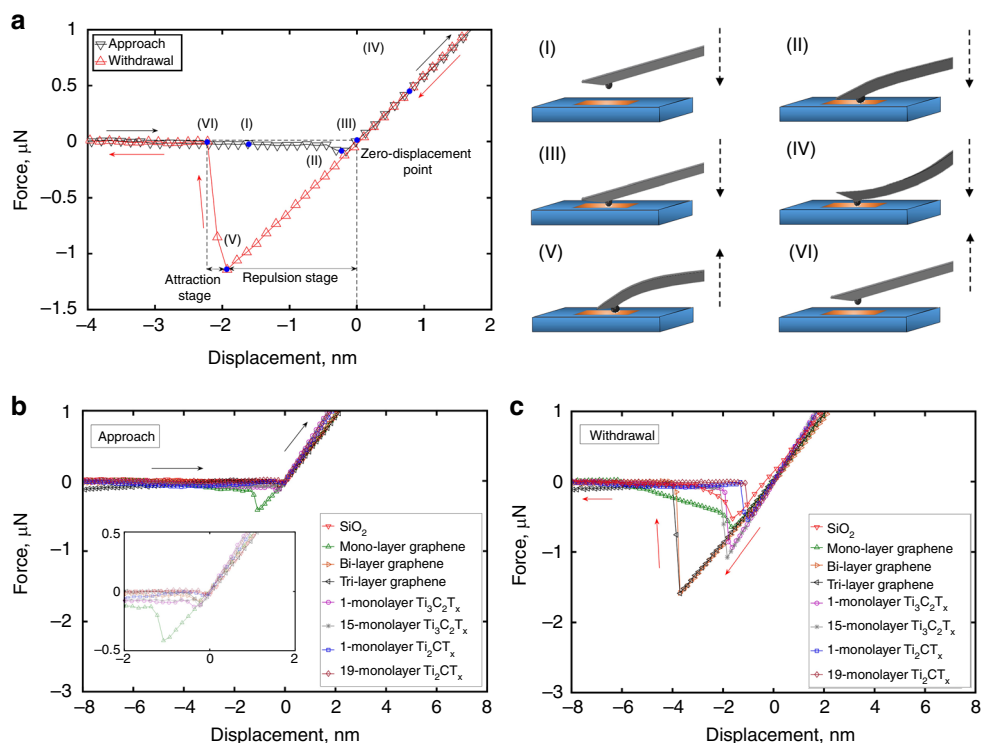


Fig. 3 Force versus displacement graphs: **a** approach and withdrawal for 5-monolayer $\text{Ti}_3\text{C}_2\text{T}_x$ sample and cartoons illustrating relative positions of the tip and the sample during different key stages of the AFM indentation process, **b** approach, **c** withdrawal for different samples

where W_{adh} is the adhesion energy per unit area, F_{adh} is the maximum adhesion force measured during the withdrawal stage, R_{tip} is the tip radius and λ is an effective coefficient that depends on the model and data used ($\lambda = 1.613$ for SiO_2 , $\lambda = 1.587, 1.543, 1.543$ for mono-layer, bi-layer, and tri-layer graphene, correspondingly, $\lambda = 1.560, 1.558$ for 1-monolayer and 15-monolayer $\text{Ti}_3\text{C}_2\text{T}_x$, and $\lambda = 1.602, 1.602$ for 1-monolayer and 19-monolayer Ti_2CT_x , correspondingly, see Supplementary Note 2). To account for the roughness effect, the tip roughness (RMS ≈ 180 pm provided by the vendor, Novascan, Inc.) and the average surface roughness of SiO_2 (65 pm), graphene (58 pm, 60 pm and 63 pm for mono-layer, bi-layer, and tri-layer graphene, respectively) and MXenes (64 pm and 78 pm for $\text{Ti}_3\text{C}_2\text{T}_x$ and Ti_2CT_x , respectively), all shown in Supplementary Fig. 3b, were employed using the modified Rumpf model^{28,29}. The actual adhesion energy is:

$$W_{\text{adh}} = \left(\frac{F_{\text{adh}}}{\lambda \pi R_{\text{tip}}} \right) \left(\frac{\left(1 + \frac{R_{\text{tip}}}{1.48R_{\text{film}}} \right)^{-1} + \left(1 + \frac{1.48R_{\text{film}}}{Z_0} \right)^{-2}}{\left(1 + \frac{R_{\text{tip}}}{1.48R_{\text{tip-RMS}}} \right)^{-1} + \left(1 + \frac{1.48R_{\text{tip-RMS}}}{Z_0} \right)^{-2}} \right) \quad (2)$$

where R_{film} is the RMS value for the sample surface, $R_{\text{tip-RMS}}$ is the RMS value for the tip and Z_0 is the equilibrium separation of two surfaces. In our experiments, the equilibrium separation Z_0 is defined as zero-force distance between the surface of SiO_2 tip and the sample surface, which was estimated to be 0.3 nm ³⁰. All adhesion energies in this work were calculated according to Eq. (2). The histograms of the adhesion energy between all sample surfaces including $\text{SiO}_2/\text{SiO}_2$, graphene/ SiO_2 , $\text{Ti}_3\text{C}_2\text{T}_x/\text{SiO}_2$, and $\text{Ti}_2\text{CT}_x/\text{SiO}_2$ are presented in Fig. 4. Gaussian fitting was applied to obtain the average adhesion energy and standard deviations for each specimen.

We compare all measurements and plot the average adhesion for each type of interactions in Fig. 5. The average adhesion

energy for $\text{SiO}_2/\text{SiO}_2$ ($0.40 \pm 0.01 \text{ J m}^{-2}$) is fairly close to the value obtained for piranha solution treated Si wafer by Na, et al. ($0.33 \pm 0.01 \text{ J m}^{-2}$)³⁰.

The adhesion energies of SiO_2 with mono-layer, bi-layer, and tri-layer graphene are 0.58 ± 0.02 , 1.36 ± 0.02 , and $1.33 \pm 0.03 \text{ J m}^{-2}$, respectively, indicating the number-of-monolayer dependence. This experimental dependence shows that adhesion energy of graphene with SiO_2 initially increases when going from mono-layer to bi-layer graphene and then stays constant when the number of graphene monolayers in the stack is increased to three. Similarly, a small increase in normal pull-off force that was more pronounced when going from 1 to 2 stacked graphene layers and less pronounced for a larger number of layers, has been predicted by modeling³¹. However, this trend was “not observed in experiments possibly due to the experimental uncertainty”³¹. Another relevant paper on the number-of-layer effect on adhesion of graphene³² mentions the opposite trend (measured by blister method), which also ceases when the number of graphene layers exceeds 2. There are also studies mentioning no number-of-layer effect on the pull-off force of graphene³³. This broad spectrum of literature results may indicate the challenges associated with experimental measurements, as well as the differences between the measurement techniques (for example, the blister method inevitably measures the effect of shear force between the material and substrate along with adhesion), and differences in graphene sample preparation (mechanically exfoliated versus CVD graphene)³². However, for the purposes of our study it is important that: (i) modeling predicts a slight increase in the adhesion with a number of graphene monolayers³¹, while it is not easy to explain the trend in opposite direction³²; and (ii) both modeling and experiments (even those where oppositely directed trend was observed) converge on that the number-of-layer trend for graphene ceases when this number exceeds 2–3, i.e., when the distance between the top-most and the bottom-most graphene layers is $\sim 0.7\text{--}1 \text{ nm}$.

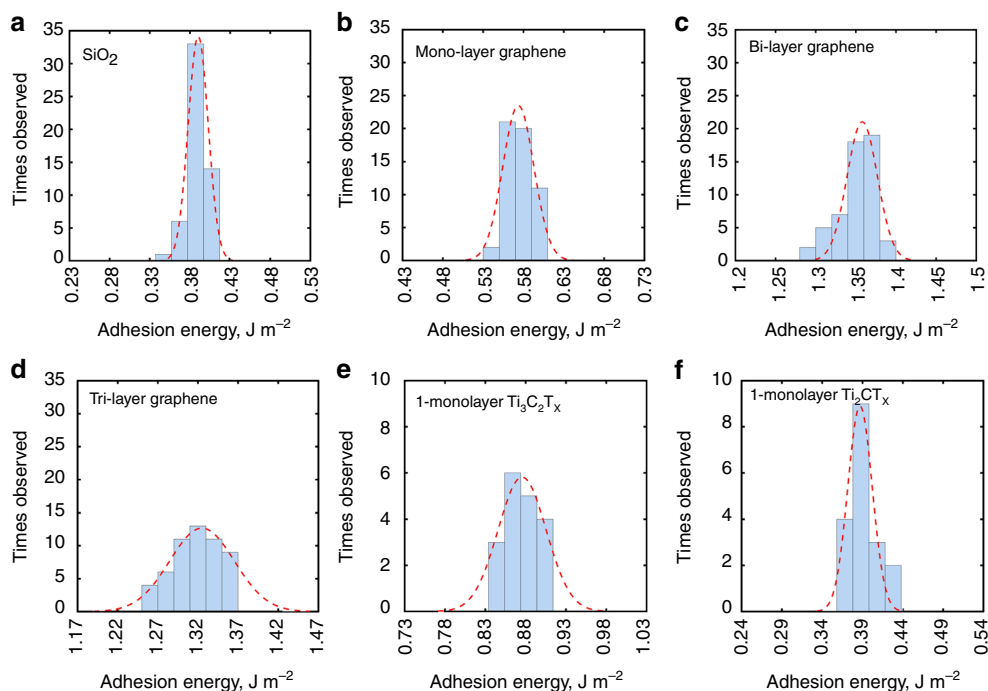


Fig. 4 Histograms of calculated adhesion energies for: **a** SiO₂/SiO₂, **b** mono-layer graphene/SiO₂, **c** bi-layer graphene/SiO₂, **d** tri-layer graphene/SiO₂, **e** 1-monolayer Ti₃C₂T_x/SiO₂, and **f** 1-monolayer Ti₂CT_x/SiO₂. (The total count is 54 for SiO₂ and graphene and 18 for MXene)

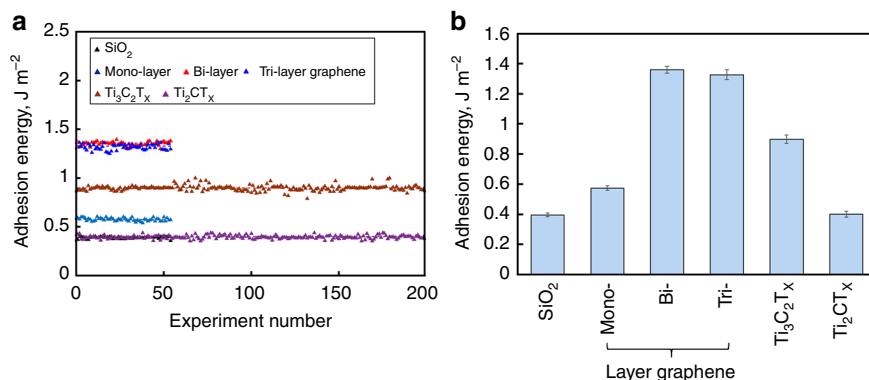


Fig. 5 **a** Adhesion energy for all measured samples (since adhesion energy of Ti₃C₂T_x and Ti₂CT_x thin films is independent of the film thickness, MXene films with different number of monolayers are represented by one symbol in the graph), **b** average adhesion energies with error bars indicating standard deviations

The average adhesion energy of the monolayer graphene measured in this work ($0.58 \pm 0.02 \text{ J m}^{-2}$) is close to the results of Jiang and Zhu ($0.46 \pm 0.02 \text{ J m}^{-2}$)²³ and Torres et al. (0.57 J m^{-2})³⁴. The small differences between these results are possibly due to different methods of graphene synthesis or different measurement methods. Jiang and Zhu measured graphene sample prepared by mechanical exfoliation, while CVD graphene was used by Torres et al. Here, we use an AFM experiment similar to Jiang and Zhu²³, while Torres et al.³⁴ measured using the nanoparticles method. Due to differences in sample preparation approaches, as well as adhesion energy measurement techniques, the authors could not provide explicit or definite reasons for the slightly higher adhesion measured in this work as compared to different literature data.

The average adhesion energy measured between SiO₂ and 1-monolayer Ti₃C₂T_x is $0.90 \pm 0.03 \text{ J m}^{-2}$, which is about twice that between SiO₂ and 1-monolayer Ti₂CT_x ($0.40 \pm 0.02 \text{ J m}^{-2}$), and larger than that between SiO₂ and monolayer graphene. At the same time, the average adhesion energy between SiO₂ and 1-monolayer Ti₂CT_x is less than between SiO₂ and monolayer

graphene (Fig. 5). Since surface chemistry of Ti₃C₂T_x and Ti₂CT_x is very similar as verified by the X-Ray photoelectron spectroscopy (XPS) (Supplementary Note 3 and Supplementary Fig. 4), we ascribe this result as mostly due to the monolayer thickness differences between the two MXenes (0.94 nm for Ti₃C₂T_x and 0.67 nm for Ti₂CT_x, respectively, calculated from X-Ray diffraction (XRD) data in Supplementary Fig. 5 and density functional theory optimized geometries in Supplementary Fig. 6). Although there was a clear monolayer thickness dependence of adhesion between each of the two MXenes and SiO₂, we did not observe any number-of-monolayer (or sample thickness) dependency (Fig. 3b, c, Fig. 5a and Supplementary Fig. 2c, d). Details of the variation of measured adhesion energies among MXenes with different thickness and from different batches can be found in Supplementary Note 4, Supplementary Table 1, Supplementary Fig. 7, and Source Data. We hypothesize that the absence of the number-of-monolayer dependence for MXene stacks may be due to a large interlayer spacing (Supplementary Figs. 5, 6), which is several times more than the interlayer spacing in stacks of

graphene. This large interlayer spacing in MXenes limits the experimentally measured adhesion by only the topmost (closest to the tip) layer contribution, preventing adhesive interactions between the underlying MXene layers and the tip. Referring to the above discussion on a number-of-monolayer dependence of adhesion for graphene, which ceases after 2–3 graphene monolayers in the stack (see also our experimental data in Fig. 5), we find that the distance at which this dependence ceases in case of stacked graphene is close to the thickness of either $\text{Ti}_3\text{C}_2\text{T}_x$ or Ti_2CT_x monolayers. It is, therefore, not surprising that no number-of-monolayer trend was observed here for the MXene samples, since their monolayer thickness and interlayer spacing are larger than those of graphene.

Discussion

The adhesion energies between SiO_2 coated Si tip and two types of MXenes were measured for the first time using AFM with a spherical tip and compared to adhesion energies between the same tip and mono-layer, bi-layer, and tri-layer graphene. The measured values are $0.90 \pm 0.03 \text{ J m}^{-2}$ and $0.40 \pm 0.02 \text{ J m}^{-2}$ for $\text{Ti}_3\text{C}_2\text{T}_x$ and Ti_2CT_x , which are in the range of adhesion between SiO_2 and graphene monolayer. A higher adhesion energy between SiO_2 and $\text{Ti}_3\text{C}_2\text{T}_x$ can be attributed to a thicker monolayer of this MXene compared to that of Ti_2CT_x . This observation provides the first illustration of how MXenes can be used to study the fundamental effects of monolayer thickness, disentangled from other factors, on mechanical properties of 2D materials. In contrast to graphene, no number-of-monolayers dependency was observed in this study for adhesion energy of multilayer MXene stacks, which we ascribe due to a larger interlayer spacing and monolayer thickness of the MXenes. The role of surface chemistry in adhesion interactions of MXenes with SiO_2 and other substrates still remains unclear, but potentially it can be used to control the adhesion in the future, provided we could better understand MXene chemistry and tailor the functional groups terminating MXene surfaces.

Methods

Atomic force microscopy (AFM). AFM (Digital Instruments Nanoscope IIIA) was conducted under the ambient conditions as illustrated in Fig. 1a. Thin films of graphene and MXene were mounted on the silicon substrate with a thin (~300 nm) layer of spontaneously formed silicon oxide. Surface profiles were measured using the tapping mode with a 3-nm radius silicon tip. The static eliminator (Static Sensing Ionizer, Keyence®) was used to neutralize any interfering electrostatic charges on the sample and/or AFM tip³⁵. A 500-nm radius colloidal silicon tip with silicon dioxide (SiO_2) surface was used to measure adhesive behavior of the samples. SEM images of the microsphere AFM tip are provided in Supplementary Fig. 8. The probe was calibrated before and after each experiment using the AFM grating to ensure that no damage to the probe occurred during the experiment. For each MXene flake, three measurements were conducted on the grid areas as illustrated in Supplementary Fig. 9a. As for graphene, nine measurements were performed on one flake due to a larger area of graphene flakes compared to MXene flakes. For further details and discussion of between the samples variations see Supplementary Note 4, Supplementary Table 2, and Source Data. The cantilever stiffness provided by the supplier (Novascan, Inc.) was $\sim 2 \text{ N m}^{-1}$. The force-displacement responses for the approach and withdrawal stages were recorded and analyzed.

The typical adhesive interaction of thin films involves the van der Waals, capillary, and electrostatic forces³⁶. The capillary force is usually induced by water bridging the sample and tip surfaces^{37,38}. We did check the effect of moisture by conducting AFM experiments with $\text{Ti}_3\text{C}_2\text{T}_x$ while varying the relative humidity (RH, Supplementary Fig. 10). The maximum fluctuation of the adhesion force is within 5% of the average value for $\text{Ti}_3\text{C}_2\text{T}_x$. These results show no significant humidity effect when RH is lower than 24%. We have also checked adhesion force versus time in air at room temperature to investigate the effect of sample oxidation. Supplementary Fig. 11a shows that the adhesion force stays constant within the first 48 h. The corresponding AFM images (Supplementary Fig. 11b) do not show any changes in the MXene surface morphology. After 48 h, the measured adhesion force drops dramatically accompanied by the visible changes in the AFM images, demonstrating signs of MXene oxidation (formation of TiO_2 etc.). This indicates that the drop in adhesion force for $\text{Ti}_3\text{C}_2\text{T}_x$ after 48 h exposure to ambient air is due to chemical changes of the MXene, emphasizing the need to work with freshly

prepared MXene samples, which was always properly taken care of in this study: all MXene samples were measured within no more than 12 h from their preparation and drying.

Synthesis of graphene and preparation of graphene samples on Si wafers.

Large-area monolayer graphene was grown by chemical vapor deposition (CVD) on $2 \times 10 \text{ cm}$ copper foils (Alfa Aesar, CAS: 7440-50-8, LOT No. P17D009). During this process, gas species were fed into the reactor flow over the $25 \mu\text{m}$ thick piece of copper foil, where hydrocarbon precursors decomposed to carbon radicals at the copper surface and then formed monolayer graphene³⁹.

To prepare the multilayer graphene, a copper foil with graphene on top was spin-coated with a layer of polymethyl methacrylate (PMMA) (3000 rpm for 30 s)⁴⁰. The foil was then etched away in $0.2 \text{ mol L}^{-1} \text{ FeCl}_3$ and $0.2 \text{ mol L}^{-1} (\text{NH}_4)_2\text{S}_2\text{O}_8$ for 2 h⁴¹. The remaining graphene/PMMA was cleaned with deionized water, transferred onto freshly synthesized graphene on copper foil and heated at 50°C in dry air to remove water. After another copper foil etching process, the graphene/graphene/PMMA sample was obtained. The tri-layer graphene was prepared by repeating this procedure. The graphene/PMMA, graphene/graphene/PMMA and graphene/graphene/graphene/PMMA samples were then transferred onto target Si (111)/ SiO_2 substrates and baked at 120°C for 15 min. Prior to transfer, Si substrates were cleaned by 30 min bath sonication in acetone and hydrophilized in piranha solution (3 mL 30% H_2O_2 slowly added to 9 mL 98% H_2SO_4) for 24 h, followed by thorough rinsing with deionized water. Finally, PMMA was removed using acetone solution, yielding a sample of graphene on the Si/ SiO_2 substrate. The residue of polymer film was etched away at 400°C in hydrogen²⁷.

Synthesis of MAX phases. Ti_3AlC_2 was prepared by pressureless synthesis method⁴². The initial powders of titanium (-325 mesh, 99%, Alfa Aesar), aluminum (-325 mesh, 99.5%, Alfa Aesar), and graphite (-325 mesh, 99%, Alfa Aesar) were ball-milled in 3:1.1:1.88 molar ratio in a polyethylene jar for 12 h at 100 rpm. Afterwards, the mixture was sintered at 1550°C for 2 h in Ar flow in an alumina boat using a tube furnace (GSL-1800X-KS60-UL, MTI Corporation). For Ti_2AlC synthesis, the initial powders of titanium carbide (typically 2-micron size, 99.5%, Alfa Aesar), titanium (-325 mesh, 99%, Alfa Aesar), and aluminum (-325 mesh, 99.5%, Alfa Aesar) were ball-milled in a molar ratio of 0.85:1.15:1.05. The mixture was then heated at 1400°C for 4 h under Ar flow in an alumina boat. The resulting ceramics were manually crushed into powders using mortar and pestle.

Preparation of MXene thin films on Si wafers. $\text{Ti}_3\text{C}_2\text{T}_x$ MXene was synthesized by selective etching of Al from Ti_3AlC_2 ⁴³. The etching was done by slowly mixing 0.3 g of Ti_3AlC_2 (-325 mesh, particle size $\leq 45 \mu\text{m}$) to the etchant, prepared by dissolving 0.3 g LiF in 6 mL of 6 M HCl in a 50 mL plastic centrifuge tube. The mix was stirred for 24 h at room temperature, followed by repeated washing with deionized water and centrifugation until the pH of supernatant reached 5.5–6.0.

$\text{Ti}_3\text{C}_2\text{T}_x$ aqueous colloidal solution was obtained via 5 min hand-shaking followed by 1 h centrifugation at 3500 rpm. $\text{Ti}_3\text{C}_2\text{T}_x$ thin films on Si were prepared from the concentrated $\text{Ti}_3\text{C}_2\text{T}_x$ colloidal solutions via interfacial film deposition method⁸. In order to prepare MXene thin films, 50–300 μL of $\text{Ti}_3\text{C}_2\text{T}_x$ colloidal solution was mixed in 50 mL DI water together with 3–6 mL toluene added during 15 min of vigorous stirring. The dispersion was then poured directly into a beaker filled with 400 mL DI water and with a few pieces of pre-cleaned Si wafers placed at the bottom. After ~ 20 min standing still, the $\text{Ti}_3\text{C}_2\text{T}_x$ film was self-assembled at the interface between water and toluene, and then the pieces of Si wafers were slowly lifted up from the solution through the interface, catching the interfacial MXene film. Finally, the MXene coated Si wafers were dried for 12 h in Ar flow at room temperature to avoid oxidation. Ti_2CT_x colloidal solutions, as well as thin films were obtained using same methods, except the MAX phase in this case was Ti_2AlC (-325 mesh, particle size $\leq 45 \mu\text{m}$) and the MXene (Ti_2CT_x) film drying time was 4 h in Ar flow at room temperature.

By adjusting the concentration of MXene colloidal solution during sample preparation, MXene films with different thicknesses were deposited ranging between 1.4 to 26.9 nm. The adhesion measurements were carried out immediately after the films were dried.

Moisture and oxidation effects. To investigate the moisture effect on adhesion measurements, three $\text{Ti}_3\text{C}_2\text{T}_x$ samples after initial drying (12 h in dry Ar flow) were placed into a closed chamber with P_2O_5 , where RH was monitored with CECOMINOD046940 monitor (Hyelec). The samples were removed for adhesion measurements when RH reached 24%, 21%, 18%, 15%, 12%, 9%, and 6% (Supplementary Fig. 10). To investigate the effect of oxidation on adhesion measurements, adhesion forces and AFM images were obtained for three $\text{Ti}_3\text{C}_2\text{T}_x$ samples exposed to air for 24–96 h (Supplementary Fig. 11).

Raman spectroscopy characterization. Raman spectroscopy was conducted using a Horiba LabRAM ARAMIS spectrometer with 632.8 nm laser. Supplementary Fig. 9b, c show Raman spectra of $\text{Ti}_3\text{C}_2\text{T}_x$ and Ti_2CT_x MXenes on Si and on cover glass. The peaks at 520 cm^{-1} recorded from MXenes deposited on Si wafer belong to Si. The MXene samples show characteristic Raman peaks of $\text{Ti}_3\text{C}_2\text{T}_x$ at 206, 270, 374, 605, and 718 cm^{-1} ^{44–46}, and of Ti_2CT_x at 200, 300, 409, and 608 cm^{-1} ⁴⁷,

respectively. All the peaks originate from Ti–C bond vibrations that are also present in the Raman spectra of respective parent MAX phases published in literature⁴⁸.

Graphene is usually characterized by G band at $\sim 1600\text{ cm}^{-1}$ and 2D band at $\sim 2650\text{ cm}^{-1}$. Raman spectra of our graphene transferred samples exhibited typical characteristics of high-quality graphene: for monolayer graphene the 2D/G intensity ratio is ~ 2.21 and a full-width at half maximum (FWHM) of 2D band is $\sim 27\text{ cm}^{-1}$ ⁴⁹. The 2D/G ratio and FWHM for the bi-layer graphene are 1 and 52 cm^{-1} , and for the tri-layer graphene, these values are 0.5 and 63 cm^{-1} ⁵⁰ (Supplementary Fig. 9d).

X-Ray diffraction characterization. The structures of $\text{Ti}_3\text{C}_2\text{T}_x$ and Ti_2CT_x MXene thin films were characterized using X-Ray Diffraction (XRD, PANalytical, Phillips MPD) with Cu K α radiation ($\lambda = 1.5406\text{ \AA}$) at $U = 45\text{ kV}$, $I = 40\text{ mA}$.

X-Ray photoelectron spectroscopy characterization. X-Ray photoelectron spectroscopy (XPS) measurements of $\text{Ti}_3\text{C}_2\text{T}_x$ and Ti_2CT_x MXene thin films were performed using a KRATOS AXIS 165 X-Ray photoelectron spectrometer with a monochromatic Al X-Ray source.

Calculation of the number of MXene monolayers. The local number of MXene monolayers in our samples was calculated from a combination of AFM and XRD data as follows. The (002) peaks for $\text{Ti}_3\text{C}_2\text{T}_x$ and Ti_2CT_x are at $2\theta = 5.98^\circ$, and 6.48° , respectively (Supplementary Fig. 5). According to Bragg's Law $2d\sin\theta = n\lambda$, the corresponding d -spacing values are 1.48 nm and 1.36 nm ^{51,52}, which are sums of the thickness of MXene monolayer and the interlayer spacing. Therefore, the number of MXene monolayers in different thin films can be calculated as the local AFM measured thickness of the films (Fig. 2) divided by the corresponding d -spacing values (Supplementary Fig. 6).

Data availability

Data available on request from the authors.

Received: 9 October 2018 Accepted: 12 June 2019

Published online: 08 July 2019

References

- Naguib, M., Mochalin, V. N., Barsoum, M. W. & Gogotsi, Y. 25th anniversary article: MXenes: a new family of two-dimensional materials. *Adv. Mater.* **26**, 992–1005 (2014).
- Anasori, B., Lukatskaya, M. R. & Gogotsi, Y. 2D metal carbides and nitrides (MXenes) for energy storage. *Nat. Rev. Mater.* **2**, 16098 (2017).
- Ghidiu, M., Lukatskaya, M. R., Zhao, M. Q., Gogotsi, Y. & Barsoum, M. W. Conductive two-dimensional titanium carbide ‘clay’ with high volumetric capacitance. *Nature* **516**, 78 (2014).
- Lukatskaya, M. R. et al. Ultra-high-rate pseudocapacitive energy storage in two-dimensional transition metal carbides. *Nat. Energy* **2**, 17105 (2017).
- Naguib, M. et al. New two-dimensional niobium and vanadium carbides as promising materials for Li-Ion batteries. *J. Am. Chem. Soc.* **135**, 15966–15969 (2013).
- Xie, Y. et al. Role of surface structure on li-ion energy storage capacity of two-dimensional transition-metal carbides. *J. Am. Chem. Soc.* **136**, 6385–6394 (2014).
- Dong, Y. et al. Metallic MXenes: a new family of materials for flexible triboelectric nanogenerators. *Nano Energy* **44**, 103–110 (2018).
- Dong, Y. et al. Saturable absorption in 2D Ti_3C_2 MXene thin films for passive photonic diodes. *Adv. Mater.* **30**, 1705714 (2018).
- Lee, E. et al. Room temperature gas sensing of two-dimensional titanium carbide (MXene). *ACS Appl. Mater. Interf.* **9**, 37184–37190 (2017).
- Chertopalov, S. & Mochalin, V. N. Environment sensitive photoresponse of spontaneously partially oxidized $\text{Ti}_3\text{C}_2\text{T}_x$ MXene thin films. *ACS Nano* **12**, 6109–6116 (2018).
- Wu, X. et al. Polymer- $\text{Ti}_3\text{C}_2\text{T}_x$ composite membranes to overcome the trade-off in solvent resistant nanofiltration for alcohol-based system. *J. Membr. Sci.* **515**, 175–188 (2016).
- Wu, Y., Nie, P., Wu, L., Dou, H. & Zhang, X. 2D MXene/SnS₂ composites as high-performance anodes for sodium ion batteries. *Chem. Eng. J.* **334**, 932–938 (2018).
- Alhabeb, M. et al. Guidelines for synthesis and processing of two-dimensional titanium carbide ($\text{Ti}_3\text{C}_2\text{T}_x$ MXene). *Chem. Mater.* **29**, 7633–7644 (2017).
- Wang, H. W., Naguib, M., Page, K., Wesolowski, D. J. & Gogotsi, Y. Resolving the structure of $\text{Ti}_3\text{C}_2\text{T}_x$ MXenes through multilevel structural modeling of the atomic pair distribution function. *Chem. Mater.* **28**, 349–359 (2015).
- Persson, I. et al. On the organization and thermal behavior of functional groups on Ti_3C_2 MXene surfaces in vacuum. *2D Mater.* **5**, 015002 (2017).
- Hope, M. A. et al. NMR reveals the surface functionalisation of Ti_3C_2 MXene. *Phys. Chem. Chem. Phys.* **18**, 5099–5102 (2016).
- Dillon, A. D. et al. Highly conductive optical quality solution-processed films of 2D titanium carbide. *Adv. Funct. Mater.* **26**, 4162–4168 (2016).
- Ling, Z. et al. Flexible and conductive MXene films and nanocomposites with high capacitance. *Proc. Natl Acad. Sci. USA* **111**, 16676–16681 (2014).
- Maleski, K., Mochalin, V. N. & Gogotsi, Y. Dispersions of two-dimensional titanium carbide MXene in organic solvents. *Chem. Mater.* **29**, 1632–1640 (2017).
- Borysiuk, V. N., Mochalin, V. N. & Gogotsi, Y. Molecular dynamic study of the mechanical properties of two-dimensional titanium carbides $\text{Ti}_n + 1\text{C}_n$ (MXenes). *Nanotechnology* **26**, 265705 (2015).
- Lipatov, A. et al. Elastic properties of 2D $\text{Ti}_3\text{C}_2\text{T}_x$ MXene monolayers and bilayers. *Sci. Adv.* **4**, eaat0491 (2018).
- Borysiuk, V. N., Mochalin, V. N. & Gogotsi, Y. Bending rigidity of two-dimensional titanium carbide (MXene) nanoribbons: a molecular dynamics study. *Comput. Mater. Sci.* **143**, 418–424 (2018).
- Jiang, T. & Zhu, Y. Measuring graphene adhesion using atomic force microscopy with a microsphere tip. *Nanoscale* **7**, 10760–10766 (2015).
- Burnham, N. A., Dominguez, D. D., Mowery, R. L. & Colton, R. J. Probing the surface forces of monolayer films with an atomic-force microscope. *Phys. Rev. Lett.* **64**, 1931–1934 (1990).
- Butt, H. J., Cappella, B. & Kappl, M. Force measurements with the atomic force microscope: technique, interpretation and applications. *Surf. Sci. Rep.* **59**, 1–152 (2005).
- Maugis, D. Adhesion of spheres: the JKR-DMT transition using a dugdale model. *J. Colloid Interface Sci.* **150**, 243–269 (1992).
- Suk, J. W. et al. Probing the adhesion interactions of graphene on silicon oxide by nanoindentation. *Carbon* **103**, 63–72 (2016).
- Jacobs, T. D. B. et al. The effect of atomic-scale roughness on the adhesion of nanoscale asperities: a combined simulation and experimental investigation. *Tribol. Lett.* **50**, 81–93 (2013).
- Rabinovich, Y. I., Adler, J. J., Ata, A., Singh, R. K. & Moudgil, B. M. Adhesion between nanoscale rough surfaces: i. role of asperity geometry. *J. Colloid Interface Sci.* **232**, 10–16 (2000).
- Na, S. R., Sarceno, D. A. & Liechti, K. M. Ultra long-range interactions between silicon surfaces. *Int. J. Solids Struct.* **80**, 168–180 (2016).
- Gong, P., Li, Q., Liu, X. Z., Carpick, R. W. & Egberts, P. Adhesion mechanics between nanoscale silicon oxide tips and few-layer graphene. *Tribol. Lett.* **65**, 61 (2017).
- Koenig, S. P., Boddeti, N. G., Dunn, M. L. & Bunch, J. S. Ultrastrong adhesion of graphene membranes. *Nat. Nanotech.* **6**, 543–546 (2011).
- Liu, X. Z., Li, Q., Egberts, P. & Carpick, R. W. Nanoscale adhesive properties of graphene: the effect of sliding history. *Adv. Mater. Interfaces* **1**, 1300053 (2014).
- Torres, J., Zhu, Y., Liu, P., Lim, S. C. & Yun, M. Adhesion energies of 2D graphene and MoS₂ to silicon and metal substrates. *Phys. Status Solidi A* **215**, 1700512 (2018).
- Ouyang, Q., Ishida, K. & Okada, K. Investigation of micro-adhesion by atomic force microscopy. *Appl. Surf. Sci.* **169**, 644–648 (2001).
- Jones, R., Pollock, H. M., Cleaver, J. A. S. & Hodges, C. S. Adhesion forces between glass and silicon surfaces in air studied by AFM: effects of relative humidity, particle size, roughness, and surface treatment. *Langmuir* **18**, 8045–8055 (2002).
- Paajanen, M., Katainen, J., Pakarinen, O. H., Foster, A. S. & Lahtinen, J. Experimental humidity dependency of small particle adhesion on silica and titania. *J. Colloid Interface Sci.* **304**, 518–523 (2006).
- Stukalov, O., Murray, C. A., Jacina, A. & Dutcher, J. R. Relative humidity control for atomic force microscopes. *Rev. Sci. Instrum.* **77**, 8153 (2006).
- Li, X. et al. Large-area synthesis of high-quality and uniform graphene films on copper foils. *Science* **324**, 1312–1314 (2009).
- Krajewska, A. et al. Fabrication and applications of multi-layer graphene stack on transparent polymer. *Appl. Phys. Lett.* **110**, 041901 (2017).
- Yoshihara, N. & Noda, M. Chemical etching of copper foils for single-layer graphene growth by chemical vapor deposition. *Chem. Phys. Lett.* **685**, 40–46 (2017).
- Huang, S. & Mochalin, V. N. Hydrolysis of 2D transition-metal carbides (MXenes) in colloidal solutions. *Inorg. Chem.* **58**, 1958–1966 (2019).
- Lipatov, A. et al. Effect of synthesis on quality, electronic properties and environmental stability of individual monolayer Ti_3C_2 MXene flakes. *Adv. Electron. Mater.* **2**, 1600255 (2016).
- Naguib, M. et al. One-step synthesis of nanocrystalline transition metal oxides on thin sheets of disordered graphitic carbon by oxidation of MXenes. *Chem. Commun.* **50**, 7420–7423 (2014).
- Cao, Y. et al. Enhanced thermal properties of poly (Vinylidene Fluoride) composites with ultrathin nanosheets of MXene. *RSC Adv.* **7**, 20494–20501 (2017).
- Zhang, C. J. et al. Oxidation stability of colloidal two-dimensional titanium carbides (MXenes). *Chem. Mater.* **29**, 4848–4856 (2017).

47. Liu, F. et al. Preparation and methane adsorption of two-dimensional carbide Ti₂C. *Adsorption* **22**, 915–922 (2016).
48. Spanier, J. E., Gupta, S., Amer, M. & Barsoum, M. W. Vibrational behavior of the Mn + 1AX_n phases from first-order Raman scattering (M = Ti, V, Cr, A = Si, X = C, N). *Phys. Rev. B* **71**, 012103 (2005).
49. Childres, et al. Raman spectroscopy of graphene and related materials. In *New Developments in Photon and Materials Research* (ed. Jang, J. I.) (Nova Science Publishers, Hauppauge, 2013).
50. Ferrari, A. C. et al. Raman spectrum of graphene and graphene layers. *Phys. Rev. Lett.* **97**, 187401 (2006).
51. Feng, W. et al. Ti₃C₂ MXene: a promising microwave absorbing material. *RSC Adv.* **8**, 2398–2403 (2018).
52. Li, X. et al. A controllable heterogeneous structure and electromagnetic wave absorption properties of Ti₂CT_x MXene. *J. Mater. Chem. C* **5**, 7621–7628 (2017).

Acknowledgements

The authors would like to thank Material Research Center at Missouri University of Science and Technology for financial support, as well as Dr. R. Brow (Missouri University of Science and Technology) for providing access to Raman spectrometer.

Author contributions

Y.X.L. and S.H.H. contributed equally to this work. C.L.W. and V.N.M. conceived and supervised the project, designed the experiments, and guided the team; Y.X.L. synthesized graphene, performed characterization, as well as adhesion measurements and data analysis; S.H.H. synthesised Ti₃T₂T_x and Ti₂CT_x MXenes, participated in adhesion measurements, performed sample characterization, as well as the data analysis; C.J.W. carried out accuracy analysis of adhesion measurements. All the authors discussed results, wrote, and commented on the paper.

Additional information

Supplementary Information accompanies this paper at <https://doi.org/10.1038/s41467-019-10982-8>.

Competing interests: The authors declare no competing interests.

Reprints and permission information is available online at <http://npg.nature.com/reprintsandpermissions/>

Peer review information: *Nature Communications* thanks Dong-Joo Kim and other anonymous reviewer(s) for their contribution to the peer review of this work.

Publisher's note: Springer Nature remains neutral with regard to jurisdictional claims in published maps and institutional affiliations.



Open Access This article is licensed under a Creative Commons Attribution 4.0 International License, which permits use, sharing, adaptation, distribution and reproduction in any medium or format, as long as you give appropriate credit to the original author(s) and the source, provide a link to the Creative Commons license, and indicate if changes were made. The images or other third party material in this article are included in the article's Creative Commons license, unless indicated otherwise in a credit line to the material. If material is not included in the article's Creative Commons license and your intended use is not permitted by statutory regulation or exceeds the permitted use, you will need to obtain permission directly from the copyright holder. To view a copy of this license, visit <http://creativecommons.org/licenses/by/4.0/>.

© The Author(s) 2019